Dalton Transactions

PAPER

View Article Online
View Journal | View Issue

Cite this: *Dalton Trans.*, 2016, **45**, 7028

A DFT study to unravel the ligand exchange kinetics and thermodynamics of Os^{VIII} oxo/hydroxido/aqua complexes in aqueous matrices†

Daniel M. E. van Niekerk, Wilhelmus J. Gerber* and Klaus R. Koch

The Os^{VIII} oxo/hydroxido complexes that are abundant in mild to relatively concentrated basic aqueous solutions are $Os^{VIII}O_4$, $[Os^{VIII}O_4(OH)]^-$ and two *cis*-$[Os^{VIII}O_4(OH)_2]^{2-}$ species. Os^{VIII} complexes that contain water ligands are thermodynamically unfavoured w.r.t. the abovementioned species. $Os^{VIII}O_4$ reacts with hydroxide in two, consecutive, elementary coordination sphere expansion steps to form the $[Os^{VIII}O_4(OH)]^-$ complex and then the *cis*-$[Os^{VIII}O_4(OH)_2]^{2-}$ species. The Gibbs energy of activation for both reactions, in the forward and reverse direction, are in the range of 6–12 kcal mol^{-1} and are relatively close to diffusion-controlled. The thermodynamic driving force of the first reaction is the bonding energy of the Os^{VIII}–OH metal-hydroxido ligand, while of the second reaction it is the relatively large hydration energy of the doubly-charged *cis*-$[Os^{VIII}O_4(OH)_2]^{2-}$ product compared to the singly-charged reactants. The DFT-calculated (PBE-D3 functional) ΔG°_{rxn} in the simulated aqueous phase (COSMO) is −2.4 kcal mol^{-1} for the first reaction and −0.6 kcal mol^{-1} for the second reaction and agree to within 1 kcal mol^{-1} with reported experimental values, at −2.7 and 0.3 kcal mol^{-1} respectively. From QTAIM and EDA analyses it is deduced that the Os^{VIII}=O bonding interactions are ionic (closed-shell) and that Os^{VIII}–OH bonding interactions are polar covalent (dative). In contrast to QTAIM, NCI analysis allowed for the identification of relatively weak intramolecular hydrogen bonding interactions between neighbouring oxo and hydroxido ligands in both $[Os^{VIII}O_4(OH)]^-$ and *cis*-$[Os^{VIII}O_4(OH)_2]^{2-}$ complexes.

Received 18th February 2016,
Accepted 14th March 2016

DOI: 10.1039/c6dt00657d

www.rsc.org/dalton

Introduction

There is extensive literature dealing with the use of $Os^{VIII}O_4$ as a homogeneous catalyst for the oxidation of several organic compounds in a variety of acidic and basic aqueous solutions.[1–8] However, when $Os^{VIII}O_4$ is extracted from CCl_4 into an aqueous hydroxide solution several possible Os^{VIII} oxo/hydroxido/aqua complexes can form.[1–3,9–12] To date, only the $Os^{VIII}O_4$ [13] and the *cis*-$[Os^{VIII}O_4(OH)_2]^{2-}$ species[14–16] have been experimentally characterised, by means of X-ray diffraction spectrometry. This leaves a window for conjecture as to what other Os^{VIII} species might exist in aqueous hydroxide solutions and which of these actually participate in reported catalytic reactions. From observed $Os^{VIII}O_4$ UV-Vis spectral changes during 'weak acid/strong base' titrations, Galbács *et al.*[2] proposed a reaction model given by eqn (1) and (2) with calculated K_{a1} and K_{a2} acid dissociation equilibrium constants, listed in Table 1.

$$OsO_2(OH)_4 + H_2O \overset{K_{a1}}{\rightleftharpoons} [OsO_3(OH)_3]^- + H_3O^+ \quad (1)$$

$$[OsO_3(OH)_3]^- + H_2O \overset{K_{a2}}{\rightleftharpoons} [OsO_4(OH)_2]^{2-} + H_3O^+ \quad (2)$$

The Os^{VIII} oxo/hydroxido complexes proposed to be in solution by Galbács *et al.*[2] are all six-coordinate complexes, $Os^{VIII}O_2(OH)_4$, $[Os^{VIII}O_3(OH)_3]^-$ and $[Os^{VIII}O_4(OH)_2]^{2-}$, with the latter presumably the *cis* stereoisomer. In addition, Griffith[12] proposed a six-coordinate species containing a water ligand, $[Os^{VIII}O_4(OH)(H_2O)]^-$. Apart from the abovementioned six-coordinate Os^{VIII} species, there is experimental support for a five-coordinate Os^{VIII} complex anion from several X-ray crystal

Table 1 Acid dissociation and the corresponding coordination sphere expansion equilibrium constants of reactions (1)–(4)

Lit.	K_{a1}	K_1	K_{a2}	K_2
1	1.3×10^{-12}	130	—	—
2	6.3×10^{-13}	63	4.0×10^{-15}	0.40
3	8.8×10^{-13}	88	7.5×10^{-15}	0.75

Department of Chemistry and Polymer Science, Stellenbosch University, Private Bag X1, Stellenbosch 7602, Western Cape, South Africa. E-mail: wgerber@sun.ac.za; Fax: +2721 808 3342; Tel: +27 21 808 2699

†Electronic supplementary information (ESI) available: Supplementary UV-Vis spectrum, additional computational results and Cartesian coordinates of all optimised structures. See DOI: 10.1039/c6dt00657d

structures of $[Os^{VIII}O_4L]$ derivatives (where L is a nitrogen donor ligand).[17] In addition, a density functional theory (DFT) (B3LYP functional) computational study by Mayer *et al.*[1] supports that a five-coordinate $[Os^{VIII}O_4(OH)]^-$ complex anion may exist in the gas phase.

If a five-coordinated $[Os^{VIII}O_4(OH)]^-$ species is present, then the reactions expected to take place are not that of a relatively weak acid reacting with water, as depicted by eqn (1) and (2), but rather coordination sphere expansion reactions (*vide infra*),[1–3,9–12] eqn (3) and (4).

$$OsO_4 + OH^- \overset{K_1}{\rightleftharpoons} [OsO_4(OH)]^- \quad (3)$$

$$[OsO_4(OH)]^- + OH^- \overset{K_2}{\rightleftharpoons} [OsO_4(OH)_2]^{2-} \quad (4)$$

The equilibrium constants of the two differing reaction schemes, (1) & (2) and (3) & (4), are mathematically related to each other as shown, for example, in eqn (5) and (6).

$$K_1 = \frac{[OsO_4(OH)^-]}{[OsO_4][OH^-]} \quad (5)$$

$$K_1K_w = \frac{[OsO_4(OH)^-][H_3O^+]}{[OsO_4]} = \frac{[OsO_3(OH)_3{}^-][H_3O^+]}{[OsO_2(OH)_4]} = K_{a1} \quad (6)$$

Although the equilibrium constants are mathematically related (eqn (6)), the actual chemical reactions are fundamentally different, giving rise to chemical species which differ significantly from a structural point of view and of course their physicochemical properties. Detailed knowledge of the chemical speciation of Os^{VIII} complexes in basic aqueous solutions is currently unclear and is of significant importance if comproportionation[11] and catalytic reactions[4–8] involving these species are to be mechanistically understood. This lack of clarity is highlighted by the variety of suggestions of what the catalytically active Os^{VIII} species could be, *e.g.* it has been reported that the catalytically active Os^{VIII} species for the oxidation of olefins[4] and of allyl alcohols[5] in mildly acidic aqueous solutions are the $Os^{VIII}O_4$ and $[H_2Os^{VIII}O_5]$ complexes respectively. Moreover, in aqueous alkaline solutions the catalytically active Os^{VIII} species for the oxidation of L-tryptophan,[6] chloramphenicol,[7] sorbitol and mannitol[8] are reported to be the $[Os^{VIII}O_4(OH)_2]^{2-}$ and/or $Os^{VIII}O_4$ complexes. To add even more complexity, Gerber *et al.*[11] reported that the oxidation of methanol and ethanol with Os^{VIII} in a 2.0 M NaOH aqueous solution results in an additional comproportionation reaction between an Os^{VIII} species and a *trans*-$[Os^{VI}O_2(OH)_4]^{2-}$ complex to form two postulated $[Os^{VII}O_3(OH)_3]^{2-}$ complexes. The formation of the Os^{VII} complex, in addition to several Os^{VIII} species, underlines the uncertainty pertaining to what the actual catalytically active osmium oxidant species in solution are likely to be.[4–8]

Electronic structure methods, and in particular density functional theory (DFT), are valuable tools used to probe chemical reactions involving transition metals.[18] If progress is to be made in understanding the mechanistic aspects of reactions in which Os^{VIII} acts as a catalyst or in terms of the synthesis of novel Os^{VIII} complexes, it is pertinent that the most abundant Os^{VIII} species should be identified under well-defined conditions. In this study we report a systematic DFT theoretical investigation of the following intertwined lines of inquiry. (i) Confirm whether the postulated chemical reactions (1) & (2) or (3) & (4) are responsible for the observed UV-Vis spectral changes reported in the literature;[2] (ii) investigate if any Os^{VIII} complexes that contain water ligands exist in appreciable quantities in solution; (iii) elucidate the nature of the metal–ligand bonding interactions as well as possible intramolecular hydrogen bonding interactions between neighbouring ligands; (iv) investigate the anticipated importance of hydration energies pertaining to the thermodynamic stability of Os^{VIII} oxo/hydroxido/aqua complexes; and (v) elucidate the kinetics of interconversion between the Os^{VIII} complexes.

Computational methods

Most calculations employed the Amsterdam Density Functional program (ADF 2012.02) developed by Baerends, Ziegler, and co-workers.[19–21] Geometries were fully optimised at the scalar-relativistic zero-order regular approximation (ZORA)[22–26] level using (i) the local density approximation (LDA)[27] functional (ii) the generalised gradient approximation (GGA) functionals PBE,[28] modified PBE (mPBE),[29] PBE that include dispersion correction terms {PBE-D,[30] PBE-D3,[31] PBE-D3(BJ)[32] and PBE-dDsC[33]}, BLYP[34–37] and BLYP that include dispersion correction terms (BLYP-D[30] and BLYP-D3[31]), PW91,[38] and (iii) the meta-GGA functional, M06L.[39,40] These calculations were done with an all-electron, quadruple-ζ plus polarisation (QZ4P) function basis set for Os and the even-tempered pVQZ basis set for O and H.[41] Optimisation in the gas phase as well as those using an implicit solvent model, namely the conductor-like screening model (COSMO),[42–45] with the parameters of water,‡ were done with the abovementioned combinations of functionals and basis sets. All of the obtained structures were characterised as potential energy surface (PES) minima or transition states by analysing the Hessian matrix.[46–50]

In order to identify the stable conformer geometries, conformational analyses were performed by monitoring the electronic energy, in a sequence of linear transit calculations (relaxed scans), as a function of the relevant σ O–Os–O–H torsion angle reaction coordinate constraint (partial convergence optimisation at each step) by systematic rotation. The resulting local minimum/minima obtained from the linear transit calculations were subsequently submitted for complete (full convergence optimisation) geometry optimisation calculations by the implementation of the abovementioned parameters and procedures.

Bonding analysis[51,52] presented in this study is further based on the ETS-NOCV approach which is a combination of the extended transition state (ETS) method with the natural

‡ ε = dielectric constant = 78.39 and Rad = radius of the rigid sphere H_2O molecules = 1.93 Å.

orbitals for chemical valence (NOCV) scheme.[53] The colour-coded NOCV deformation-density contributions were generated with the ADF graphical user interface (GUI).[54]

Both the quantum theory of atoms in molecules (QTAIM)[55,56] and the non-covalent interactions (NCI)[57] analyses were done using the AIMAll software package[58] on geometry optimised structures that were obtained with ADF.[19–21] Wavefunctional files (.wfx) used for QTAIM analysis were created using Gaussian 09,[59] with an effective core potential (ECP) basis set, Lanl2DZ,[60–62] for Os and the correlation-consistent, cc-pVQZ,[63] basis set for O and H. The conductor-like polarisable continuum model (CPCM)[64,65] was used to account for aqueous solvation effects.

Experimental details

Materials

Batches of high purity potassium osmate crystals, $K_2[Os^{VI}O_2(OH)_4]$, were obtained from Anglo Platinum Ltd (South Africa). Sodium hydroxide salts (Sigma-Aldrich) were of analytical reagent grade. Analytical grade orthophosphoric acid (H_3PO_4), hydrogen peroxide (H_2O_2) and carbon tetrachloride (CCl_4) (Merck Chemicals) were used in the preparation of osmium tetroxide $Os^{VIII}O_4$ stock solutions. Aqueous $Os^{VIII}O_4$ solutions were prepared and diluted to the desired concentration using MilliQ water with a resistivity of 18.2 MΩ cm.

Preparation of $Os^{VIII}O_4$ solutions

$Os^{VIII}O_4$ solutions were prepared by oxidative distillation of the pure $K_2[Os^{VI}O_2(OH)_4]$ salt using 10% (v/v) H_2O_2 in an aqueous 45% (v/v) H_3PO_4 matrix. The evolved $Os^{VIII}O_4$ vapour was trapped in CCl_4. The UV-Vis spectrum of the obtained $Os^{VIII}O_4$ in CCl_4 was identical to that reported in literature,[11,66,67] ESI Fig. S1,† and confirmed that only $Os^{VIII}O_4$ was present in CCl_4. Aqueous $Os^{VIII}O_4$ solutions were prepared by extraction of $Os^{VIII}O_4$ into MilliQ water.

Instrumentation

Stopped-flow UV-Vis spectra were recorded using Applied Photophysics' SF.3 stopped-flow accessory and Chirascan™-plus circular dichroism spectrometer and the obtained data was processed with Applied Photophysics' Pro-Data software.

Results and discussion

Thermodynamic and metal–ligand bonding analyses of Os^{VIII} oxo/hydroxido/aqua complexes

The wavelengths at which the UV-Vis absorption maxima of $Os^{VIII}O_4$ occur in condensed phases such as water and carbon tetrachloride (CCl_4) and in the gas phase are essentially identical, Fig. S1,† [11] apart from the broader absorption lines in the solvent phases. The agreement of absorption maxima observed in these phases as a function of wavelength provides compelling evidence that $Os^{VIII}O_4$ does not react with water to form

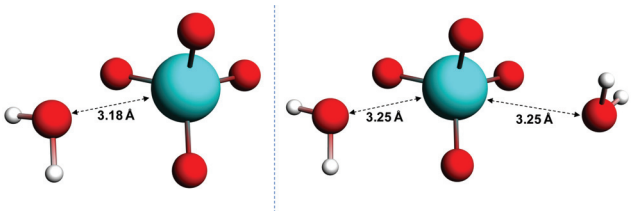

Fig. 1 Converged geometries of $[Os^{VIII}O_4]\cdot H_2O$ (left) and $[Os^{VIII}O_4]\cdot 2H_2O$ (right) in the simulated aqueous phase (PBE functional).

Os^{VIII} complexes with coordinated water ligands. Nonetheless, several hypothetical five- and six-coordinate Os^{VIII} aqua complexes, *e.g.* $[Os^{VIII}O_4(H_2O)]$, *cis*-$[Os^{VIII}O_4(H_2O)_2]$ and *trans*-$[Os^{VIII}O_4(H_2O)_2]$, were submitted for geometry optimisation and subsequent vibrational frequencies analysis calculations. In the gas phase, the Os–water "ligand" distance increases with each self-consistent field (SCF) iteration until unphysical bond lengths are observed (>7.0 Å). This "trend" was observed using a variety of DFT functionals (LDA, several GGA's and one MetaGGA); with the inclusion or exclusion of relativistic effects (ZORA) and irrespective of basis set quality. Conversely, in the simulated aqueous phase the geometries converge, Fig. 1, where the $O_4Os^{VIII}\cdots OH_2$ distances are 3.18 Å and 3.25 Å in the $[Os^{VIII}O_4]\cdot H_2O$ and $[Os^{VIII}O_4]\cdot 2H_2O$ structures respectively. However, one negative frequency, corresponding to a bending (rocking) motion of H_2O, was obtained for both the $[Os^{VIII}O_4]\cdot H_2O$ and $[Os^{VIII}O_4]\cdot 2H_2O$ structures, despite performing both the geometry optimisation and frequencies analysis calculations at the highest available integration accuracy. From these results it is reasonable to conclude that there are no minima on the multidimensional potential energy surface (PES) w.r.t. Os^{VIII} complexes that have coordinated water ligands. This corroborates the conclusion from the essentially identical UV-Vis spectra of $Os^{VIII}O_4$ obtained in various solvents and in the gas phase. Moreover, the hypothetical osmium(VIII) acid, $Os^{VIII}O_2(OH)_4$, and $[Os^{VIII}O_4(OH)(H_2O)]^-$ species proposed by Galbács *et al.*[2] and Griffith[12] respectively, Fig. S2 and S3,† are thermodynamically much less favoured w.r.t. the found Os^{VIII} oxo/hydroxido species associated with reaction scheme (3) & (4) (*vide infra*).§

In contrast to the abovementioned Os^{VIII} aqua complexes, equilibrium geometries of the Os^{VIII} species depicted by eqn (3) and (4) were found relatively easily in both the gas and simulated aqueous phase. The molecular graphs of $Os^{VIII}O_4$, $[Os^{VIII}O_4(OH)]^-$, *cis*$_1$-$[Os^{VIII}O_4(OH)_2]^{2-}$, *cis*$_2$-$[Os^{VIII}O_4(OH)_2]^{2-}$ and *trans*-$[Os^{VIII}O_4(OH)_2]^{2-}$ are shown in Fig. 2.

Comparison of experimentally obtained IR vibrational frequencies and Os–O bond lengths of $Os^{VIII}O_4$ [13,68,69] agrees well with that obtained from the DFT calculations, Tables 2 and 3, supporting the computational methodology.

A detailed conformational analysis of the five-coordinate $[Os^{VIII}O_4(OH)]^-$ species reveals only one stable equilibrium

§ Detailed DFT calculations are presented and discussed in the ESI.†

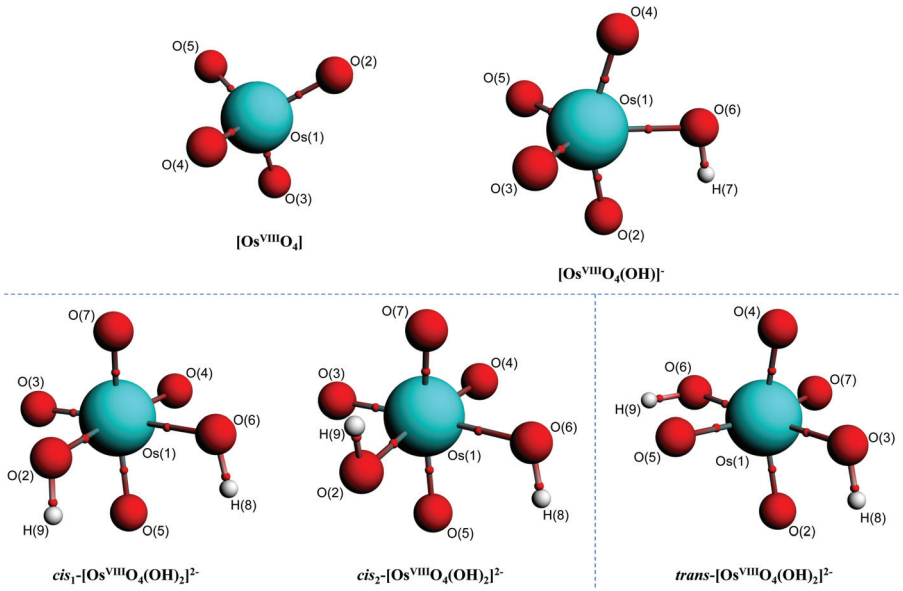

Fig. 2 Molecular graphs of stable Os^{VIII} oxo/hydroxido structures in the simulated aqueous phase (PBE functional) pertaining to eqn (3) and (4) with small red spheres representing (3, −1) critical points.

Table 2 Computed and experimental harmonic frequencies of $Os^{VIII}O_4$ (cm^{-1})

Mode i	Computed (PBE)		Experimental[68]
	Gas phase	COSMO (aqueous)	Gas phase (observed)
1 (A_1)	985.1	984.2	965.2
2 (E)	333.3	326.2	333.1
3 (T_2)	968.2	941.7	960.5
4 (T_2)	329.9	313.9	329.0

Table 3 Computed and experimental Os=O bond length of $Os^{VIII}O_4$ (Å)

Computed (PBE)		Experimental		
Gas phase	COSMO (aqueous)	Gas phase[69]	Crystallographic[13]	
1.7125	1.7115	1.712 (3)	1.684 (7)	1.710 (7)

Table 4 Calculated standard reaction Gibbs free energies in kcal mol^{-1} and equilibrium constants of reaction (3) at 298.15 K

Functional	Gas phase		COSMO (aqueous)	
	ΔG°_{rxn}	K_1	ΔG°_{rxn}	K_1
LDA	−58.9	1.6×10^{43}	−15.6	2.8×10^{11}
PBE	−45.8	3.5×10^{33}	−1.6	15.0
PBE-D	−46.4	9.6×10^{33}	−1.2	7.5
PBE-D3	−46.3	8.7×10^{33}	−2.4	59.2
PBE-D3(BJ)	−47.0	2.9×10^{34}	−3.0	1.6×10^{2}
PBE-dDsC	−46.9	2.3×10^{34}	−2.8	1.2×10^{2}
mPBE	−44.0	1.7×10^{32}	0.2	0.7
BLYP	−41.5	2.5×10^{30}	4.5	5.1×10^{-4}
BLYP-D	−41.1	1.3×10^{30}	3.4	3.1×10^{-3}
BLYP-D3	−41.2	1.5×10^{30}	3.4	3.4×10^{-3}
PW91	−46.9	2.5×10^{34}	−2.7	95.3
M06L	−45.1	1.2×10^{33}	−1.0	5.2
Experimental[a]			**−2.7**	**93.7**

[a] Calculated average experimental value taken from ref. 1–3.

geometry, shown in Fig. 2, with a coordinated hydroxido ligand positioned pseudo-equatorially. The equilibrium constants listed in Table 1 can be compared to our DFT-calculated values of the coordination sphere expansion reaction, eqn (3), in order to establish its validity. Our calculated ΔG°_{rxn} of reaction (3), Table 4, in the gas phase compare poorly with experiment (K_1 is overestimated by thirty to forty orders of magnitude) for all the functionals used. This explains why Mayer *et al.*[1] do not report their gas phase, DFT-calculated equilibrium constants to compare with the available experimental data. By contrast, apart from the LDA functional, the agreement between experiment and DFT-calculated ΔG°_{rxn} in the simulated aqueous phase is, in our opinion, excellent considering the relatively small average experimental ΔG°_{rxn} of approximately −2.7 kcal mol^{-1}.[1–3]

It may, however, be argued that the calculated values obtained by BLYP, BLYP-D and BLYP-D3 compare poorly with experiment value since they do not have the correct sign of ΔG°_{rxn} w.r.t. reaction (3). This is not problematic if the following is taken into account and to simplify the discussion we consider a relatively easy to conceptualise reaction (7).

$$A \overset{K_{ex}}{\rightleftharpoons} B \quad (7)$$

If K_{ex} is equal to one there is a 1 : 1 concentration ratio of A and B, and ΔG°_{rxn} of reaction (7) is equal to zero. If the

concentration ratio of A and B is 0.4 : 0.6, then K_{ex} is equal to 1.5 and ΔG°_{rxn} has a slight negative value equalling −1.005 kJ mol^{-1}. By contrast, if the concentration ratio of A and B is 0.6 : 0.4 the K_{ex} is equal to 0.66 and ΔG°_{rxn} has a slight positive number of 1.005 kJ mol^{-1}. Even though ΔG°_{rxn} is now positive a significant amount of B is still present at equilibrium. The same argument holds for reaction (3) w.r.t. the positive BLYP, BLYP-D and BLYP-D3 ΔG°_{rxn} 's obtained and therefore the agreement with experiment is actually quite good.

The agreement between DFT and experiment,[1–3] Table 4, provides strong support for the formation of a five-coordinate $[Os^{VIII}O_4(OH)]^-$ species. Moreover, in the gas phase the DFT computational results largely favour the formation of a five-coordinate $[Os^{VIII}O_4(OH)]^-$ species ($\Delta G^{\circ}_{rxn} \approx -46$ kcal mol^{-1}) whereas in the simulated aqueous phase, COSMO, the ΔG°_{rxn} is a relatively small negative or positive number, Table 4. This suggests that hydration energy plays a large role in decreasing the relative thermodynamic stability of the $[Os^{VIII}O_4(OH)]^-$ species w.r.t. the reactants. The COSMO calculated hydration energies of $Os^{VIII}O_4$, OH^- and $[Os^{VIII}O_4(OH)]^-$ are −10.3, −96.1 and −58.9 kcal mol^{-1} (PBE functional) respectively. The relatively large hydration energy of the high charge density hydroxide anion compared to the other species decreases the gas phase ΔG°_{rxn} of reaction (3) by approximately 40–47 kcal mol^{-1}, depending on the functional used. Considering the above, the thermodynamic driving force of reaction (3) is the bonding energy of a hydroxido ligand with Os. For further insight pertaining to the bonding energy and types of bonding interactions occurring between the $Os^{VIII}O_4$ and OH^- moieties we performed an energy decomposition analysis (EDA) as proposed by Rauk and Ziegler.[51,52] Although Bader criticises energy partition schemes,[70] due to fact that unique partitioning cannot be performed, there are many examples, notably by Frenking,[71] where chemical insight and estimation of bond dissociation energies can be obtained to describe the physical properties of the chemical system at hand. The bond dissociation energy, $-D_e$, between two fragments Q and P (Q = $Os^{VIII}O_4$, P = OH^-) consist of two main energetic contributions (in the gas phase), namely the interaction (ΔE_{int}) and preparation energy (ΔE_{prep}), eqn (8). ΔE_{prep} is also known as the 'deformation energy' and is the electronic energy difference between the prepared fragments, *i.e.* as Q and P occur in compound QP, and the fragments Q and P present in their equilibrium geometry. However, for EDA done in a simulated aqueous phase a third term, ΔE_{solv}, must also be included to account for the total change in solvation energy between compound QP and fragments Q and P as they occur in their equilibrium geometry, eqn (8). The ADF software[19–21] does not automatically calculate ΔE_{solv}; it only prints out E_{solv} of QP for an EDA calculation. ΔE_{solv} is therefore obtained manually by subtracting the solvation energies of Q and P (equilibrium geometries) from that of QP. It should be noted that Cramer *et al.*[72] also include solvation energy in their EDA calculations but do not specify how ΔE_{solv} is calculated, *i.e.* whether the reported values are the energy difference between compound QP and the equilibrium or the 'deformed' geometries of fragments Q and P.

$$-D_e = \Delta E_{int} + \Delta E_{prep}(+\Delta E_{solv}) \quad (8)$$

The ΔE_{int} term between two fragments is defined as the sum of several main energetic contributions, eqn (9).

$$\Delta E_{int} = \Delta E_{Pauli} + \Delta E_{elstat} + \Delta E_{orb} + \Delta E_{disp} \quad (9)$$

The first two terms of ΔE_{int}, eqn (9), are computed by using the unperturbed fragments and account for the Pauli (steric) repulsion (ΔE_{Pauli}) and electrostatic interaction (ΔE_{elstat}), whilst the third term (ΔE_{orb}) represents the energy 'released' when the fragment electron densities are allowed to relax to their equilibrium electron densities. For covalent bonds the absolute value of ΔE_{orb} is larger than ΔE_{elstat}, while the opposite holds true for ionic bonds. Dispersion energy (ΔE_{disp}) makes up the fourth contribution to the total ΔE_{int}. It should be noted that the energy decomposition analysis is dependent on the nature and structure of the chosen fragments, especially for charged species, which makes the determination of the relative ionicity/covalency of the Os^{VIII}–OH bond challenging.[72] This is discussed further when the topological analysis of the electron density using the QTAIM method is presented (*vide infra*). The EDA results obtained using the above approach for the $[Os^{VIII}O_4(OH)]^-$ anion were done in both gas and simulated aqueous phases, Table 5.

The calculated values of ΔE_{Pauli}, ΔE_{elstat} and ΔE_{orb} differ by less than approximately 2.1 kcal mol^{-1} in both the gas and simulated aqueous phase while ΔE_{disp}, as obtained by four different dispersion correction methods, contributes only

Table 5 EDA (kcal mol^{-1}) of the Os^{VIII}–OH ligand bond of $[Os^{VIII}O_4(OH)]^-$ in the gas and simulated aqueous phase

Functional	Phase	ΔE_{int}	ΔE_{Pauli}	ΔE_{elstat}	ΔE_{orb}	ΔE_{disp}	ΔE_{solv}	ΔE_{prep}	$-D_e$
PBE	Gas	−105.0	270.5	−241.6	−133.9	—	—	48.7	−56.2
	Aqueous	−103.8	270.7	−242.3	−132.1	—	47.4	44.6	−11.8
PBE-D	Gas	−105.6	267.6	−239.6	−133.0	−0.7	—	48.9	−56.7
	Aqueous	−104.5	268.2	−240.6	−131.4	−0.7	47.4	44.7	−12.4
PBE-D3	Gas	−105.6	269.8	−241.1	−133.6	−0.6	—	48.9	−56.7
	Aqueous	−104.4	270.1	−242.0	−132.0	−0.6	47.4	44.6	−12.4
PBE-D3(BJ)	Gas	−106.2	272.1	−242.6	−134.4	−1.2	—	48.8	−57.4
	Aqueous	−105.0	271.9	−243.1	−132.6	−1.2	47.4	44.6	−13.0
PBE-dDsC	Gas	−105.9	273.2	−243.4	−134.7	−1.0	—	48.6	−57.3
	Aqueous	−104.5	272.6	−243.4	−132.6	−1.0	47.4	44.2	−12.8

minimally to ΔE_{int}. In both the gas and simulated aqueous phase approximately two-thirds of the stabilisation of the Os^{VIII}–OH metal-hydroxido bond is due to electrostatic contributions which reflect its ionic character. The ratio of $\Delta E_{elstat} : \Delta E_{orb}$ remains approximately 1.8 regardless of whether the analysis is done in the gas or simulated aqueous phase. It is the ΔE_{solv} contribution, of approximately 47.4 kcal mol^{-1}, which dramatically changes $-D_e$ in the simulated aqueous phase, from approximately −57 to −12 kcal mol^{-1}. However, since the calculated $-D_e$ values are negative in both phases, solvation (hydration) energy is not an essential component to promote the formation of the metal-hydroxido bond in $[Os^{VIII}O_4(OH)]^-$. Taking these factors into account leads to the same conclusion mentioned previously, that reaction (3) is thermodynamically driven by the bonding energy of the Os^{VIII}–OH metal-hydroxido ligand.

The covalent aspects of the Os^{VIII}–OH metal-hydroxido bond was further analysed by using ETS-NOCV which is a combined charge and energy decomposition scheme for bond analysis.[53] The ΔE_{orb} stabilising contribution, Table 5, representing the interactions between the occupied molecular orbitals of one fragment with the unoccupied molecular orbitals of the other fragment, is linked to the electronic bonding effect from the formation of a chemical bond. ETS-NOCV yields the contributions from the different natural orbitals (constructed from the fragment orbitals) to the total orbitalic contribution.

The sum of the calculated energies of the two major deformation-density channels, $\Delta\rho_1$ and $\Delta\rho_2$, to the covalent contribution of the Os^{VIII}–OH bond energy make up approximately 85% of the total orbitalic energy stabilisation, Table 6.

The two highest deformation-density channels, $\Delta\rho_1$ and $\Delta\rho_2$, are shown in Fig. 3. They are approximately −91.5 (69%) and −21.2 (16%) kcal mol^{-1} and correspond to σ- and π-donations respectively, from the occupied 2p orbitals of the hydroxido oxygen to the empty 5d orbitals of the osmium metal-centre.

To investigate reaction (4) in more detail, conformational analyses using relaxed potential energy scans were performed in order to identify equilibrium structures of the six-coordinate Os^{VIII} species. Three stable equilibrium geometries were found, two *cis* and one *trans* structure, as shown in Fig. 2. A diagram that briefly summarises the three possible coordination sphere expansion reactions and the stereoisomer interchange of the three six-coordinate Os^{VIII} oxo/hydroxido species are shown in Scheme 1.

Table 6 ETS-NOCV calculated energies (kcal mol^{-1}), in the simulated aqueous phase, of the two highest deformation-density contributions, $\Delta\rho_1$ and $\Delta\rho_2$, of the Os^{VIII}–OH bond in $[Os^{VIII}O_4(OH)]^-$

Functional	$\Delta\rho_1$	$\Delta\rho_2$	ΔE_{orb}
PBE	−91.5 (69.3%)	−21.2 (16.0%)	−132.1
PBE-D	−91.0 (69.3%)	−21.1 (16.1%)	−131.4
PBE-D3	−91.4 (69.3%)	−21.2 (16.0%)	−132.0
PBE-D3(BJ)	−91.8 (69.3%)	−21.3 (16.0%)	−132.6
PBE-dDsC	−91.8 (69.2%)	−21.3 (16.0%)	−132.6

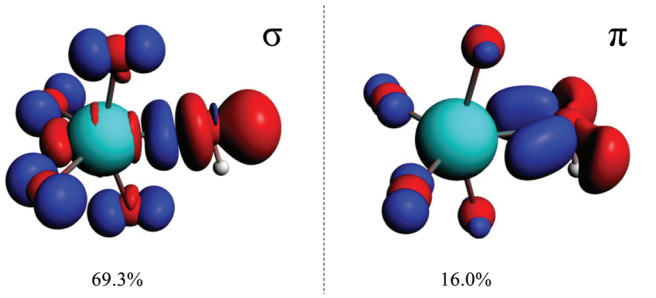

Fig. 3 Natural orbitals for the Chemical Valence (NOCV) showing the two largest contributions to the orbitalic energy of each of the Os^{VIII}–OH interactions of $[Os^{VIII}O_4(OH)]^-$ in the simulated aqueous phase with the PBE functional (contribution presented as percentage of the total orbitalic interaction energy). Red and blue colouring corresponds to regions of local charge depletion and accumulation respectively.

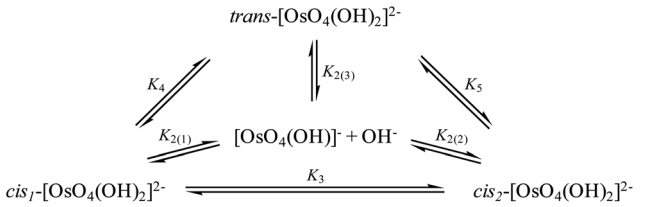

Scheme 1 Coordination sphere expansion reactions of $[Os^{VIII}O_4(OH)]^-$ ($K_{2(1)}$, $K_{2(2)}$ and $K_{2(3)}$) and stereoisomer interchange reactions of $[Os^{VIII}O_4(OH)_2]^{2-}$ species (K_3, K_4 and K_5).

The DFT-calculated equilibrium constants of the isomerisation reactions (10) and (11) are K_3 = 1.03 and K_4 = 1.0 × 10^6 respectively, *i.e.* the two *cis* conformations are approximately 10 kcal mol^{-1} thermodynamically more stable than the *trans*-species. The ratio of *cis*- to *trans*-$[Os^{VIII}O_4(OH)_2]^{2-}$ species is approximately a million to one and therefore the *trans* species is not taken into account when the second coordination sphere expansion of the five-coordinate $[Os^{VIII}O_4(OH)]^-$ to the six-coordinate $[Os^{VIII}O_4(OH)_2]^{2-}$ species is discussed below.

$$cis_1\text{-}[OsO_4(OH)_2]^{2-} \overset{K_3}{\rightleftharpoons} cis_2\text{-}[OsO_4(OH)_2]^{2-} \quad (10)$$

$$trans\text{-}[OsO_4(OH)_2]^{2-} \overset{K_4}{\rightleftharpoons} cis_1\text{-}[OsO_4(OH)_2]^{2-} \quad (11)$$

Experimentally, the two *cis*-$[Os^{VIII}O_4(OH)_2]^{2-}$ species in solution cannot be distinguished from one another. Therefore, in order to calculate K_2 by means of DFT, eqn (4) has to be re-written as shown in eqn (12) and (13). Addition of the equilibrium expressions associated with eqn (12) and (13) results in eqn (14) which relates the equilibrium constant of eqn (4) with those in eqn (12) and (13). The associated standard reaction Gibbs free energy of the second coordination sphere expansion of the five-coordinate $[Os^{VIII}O_4(OH)]^-$ to the six-coordinate $[Os^{VIII}O_4(OH)_2]^{2-}$ species is given by eqn (15).

$$[OsO_4(OH)]^- + OH^- \overset{K_{2(1)}}{\rightleftharpoons} cis_1\text{-}[OsO_4(OH)_2]^{2-} \quad (12)$$

$$[OsO_4(OH)]^- + OH^- \overset{K_{2(2)}}{\rightleftharpoons} cis_2\text{-}[OsO_4(OH)_2]^{2-} \quad (13)$$

$$K_{2(1)} + K_{2(2)} = \frac{cis_1\text{-}[OsO_4(OH)_2{}^{2-}]}{[OsO_4(OH)^-][OH^-]} + \frac{cis_2\text{-}[OsO_4(OH)_2{}^{2-}]}{[OsO_4(OH)^-][OH^-]} = \frac{[OsO_4(OH)_2{}^{2-}]}{[OsO_4(OH)^-][OH^-]} = K_2 \quad (14)$$

where $cis_1\text{-}[OsO_4(OH)_2{}^{2-}] + cis_2\text{-}[OsO_4(OH)_2{}^{2-}] = [OsO_4(OH)_2{}^{2-}]$

$$\Delta G^\circ_{rxn} = -RT\ln\{K_{2(1)} + K_{2(2)}\} = -RT\ln(K_2) \quad (15)$$

In the gas phase the calculated ΔG°_{rxn} values of reaction (4) (12, 13) are large and positive, Table 7, in contrast to the large negative values of reaction (3). Conversely, the agreement between experimental and DFT-calculated standard reaction Gibbs free energies in the simulated aqueous phase are excellent, excluding the LDA functional. The hydration energies (PBE functional) of the doubly-charged cis_1- and cis_2-$[Os^{VIII}O_4(OH)_2]^{2-}$ species are −219.4 and −218.0 kcal mol^{-1} respectively and are relatively large compared to the hydration energies of $[OH]^-$ and $[Os^{VIII}O_4(OH)]^-$, −96.1 and −58.9 kcal mol^{-1} respectively. This implies that the hydration energy of the *cis*-$[Os^{VIII}O_4(OH)_2]^{2-}$ species is the thermodynamic driving force of reaction (4). The good agreement between experimental[2,3] and calculated thermodynamic parameters provides good evidence that the Os^{VIII} species present in basic aqueous solutions are $Os^{VIII}O_4$, $[Os^{VIII}O_4(OH)]^-$ and two *cis*-$[Os^{VIII}O_4(OH)_2]^{2-}$ complexes, *i.e.* reactions (3) & (4) and not reactions (1) & (2).

The results of EDA calculations performed on the Os^{VIII}–OH bonds of the three six-coordinate $[Os^{VIII}O_4(OH)_2]^{2-}$ species are encapsulated in Table 8. The two hydroxido ligands in each of the three complex species are indistinguishable from one another due to their spatial symmetry and therefore the $-D_e$ values of the bonds of both ligands are the same.

In contrast to the Os^{VIII}–OH bonding energetics in the $[Os^{VIII}O_4(OH)]^-$ complex, the stabilisation contributions from the orbitalic and electrostatic interactions of all three $[Os^{VIII}O_4(OH)_2]^{2-}$ complexes are not large enough to yield negative ΔE_{int} values. The large positive $-D_e$ values reflect why large positive calculated ΔG°_{rxn} values in the gas phase, Table 7, were obtained. The ratio of $\Delta E_{elstat} : \Delta E_{orb}$ in each of the two *cis*-$[Os^{VIII}O_4(OH)_2]^{2-}$ complex species is approximately 0.83 and 0.92 in the gas and simulated aqueous phase respectively and approximately 0.95 and 1.05 for the *trans*-$[Os^{VIII}O_4(OH)_2]^{2-}$ complex in the gas and simulated aqueous phase. The Os^{VIII}–OH bonding interaction has slightly less covalent character in the *trans*-compared to the *cis*-$[Os^{VIII}O_4(OH)_2]^{2-}$ species. The ΔE_{elstat} stabilisation of the Os^{VIII}–OH interaction of all three species is less compared to that of $[Os^{VIII}O_4(OH)]^-$ since the two fragments involved are now both anionic, resulting in less attraction as compared to when only one fragment is negatively charged. Similarly to that of the $[Os^{VIII}O_4(OH)]^-$ complex, contributions of ΔE_{disp} are minimal for all three complexes. Despite the fact that the *trans*-$[Os^{VIII}O_4(OH)_2]^{2-}$ complex has a more favourable ΔE_{int} compared to that of the two *cis*-$[Os^{VIII}O_4(OH)_2]^{2-}$ species, it is the significantly larger deformation energy contribution which makes $-D_e$, and also the relative stability of the *trans*-$[Os^{VIII}O_4(OH)_2]^{2-}$ complex, less than that of the two *cis*-$[Os^{VIII}O_4(OH)_2]^{2-}$ species. The bond dissociation energy of the *trans*-$[Os^{VIII}O_4(OH)_2]^{2-}$ species is approximately 9–10 kcal mol^{-1} less favourable (gas or simulated aqueous phase) compared to the two *cis*-$[Os^{VIII}O_4(OH)_2]^{2-}$ species. EDA analysis therefore provides a reason why the *trans*-$[Os^{VIII}O_4(OH)_2]^{2-}$ complex is thermodynamically less stable compared to the two *cis*-$[Os^{VIII}O_4(OH)_2]^{2-}$ species. The calculated $-D_e$ values in the gas phase are relatively large positive values meaning that formation of the second Os^{VIII}–OH metal-hydroxido bond is thermodynamically unfavourable in the absence of an adequate solvation (hydration) energy contribution. It is only when the hydration energy, ΔE_{solv} contribution, is present that negative $-D_e$ values are obtained. Therefore, in contrast to reaction (3), reaction (4) is thermodynamically driven by the larger hydration energy of the doubly-charged $[Os^{VIII}O_4(OH)_2]^{2-}$ species in comparison with that of the two, singly-charged reactants, *i.e.* $[Os^{VIII}O_4(OH)]^-$ and a hydroxide anion.

Calculated results of ETS-NOCV analysis of the Os^{VIII}–OH bond in the three six-coordinate $[Os^{VIII}O_4(OH)_2]^{2-}$ species are similar to that obtained in the five-coordinate $[Os^{VIII}O_4(OH)]^-$ species. The sum of the calculated energies of the two major deformation-density channels, $\Delta\rho_1$ and $\Delta\rho_2$, to the covalent contribution of the Os^{VIII}–OH bond energy make up approximately 71% and 16% respectively of the total orbitalic stabilisation, Table S1,† and correspond to σ- and π-donations respectively, from the occupied 2p orbitals of the hydroxido oxygen to the empty 5d orbitals of the osmium metal-centre, Fig. S4.†

To further characterise the nature of the Os^{VIII}-oxo/hydroxido bonding interactions and to investigate whether possible intramolecular interactions occur, we performed a topological analysis of the electron density according to the quantum theory of atoms in molecules (QTAIM).[55,56] The definition for

Table 7 Calculated standard reaction Gibbs free energies in kcal mol^{-1} and equilibrium constants of reaction (4) at 298.15 K

	Gas phase		COSMO (aqueous)	
Functional	ΔG°_{rxn}	K_{eq}	ΔG°_{rxn}	K_{eq}
LDA	52.4	3.9×10^{-39}	−10.8	8.1×10^{7}
PBE	62.0	3.4×10^{-46}	−0.0(3)	1.1
PBE-D	60.0	9.9×10^{-45}	−2.6	82.2
PBE-D3	60.9	2.3×10^{-45}	−0.6	2.8
PBE-D3(BJ)	60.9	2.2×10^{-45}	−0.9	5.0
PBE-dDsC	60.6	3.9×10^{-45}	−1.1	6.9
mPBE	63.1	5.9×10^{-47}	1.5	8.2×10^{-2}
BLYP	65.3	1.5×10^{-48}	3.1	5.1×10^{-3}
BLYP-D	60.4	5.3×10^{-45}	−0.3	1.7
BLYP-D3	61.0	1.8×10^{-45}	0.4	0.5
PW91	60.8	2.6×10^{-45}	−1.0	5.2
M06L	59.7	1.6×10^{-44}	−3.9	7.5×10^{2}
Experimental[a]			**0.3**	**0.6**

[a] Calculated average experimental value taken from ref. 2 and 3.

Table 8 EDA (kcal mol^{-1}) of the Os^{VIII}–OH ligand bond of [Os^{VIII}O$_4$(OH)$_2$]$^{2-}$ complexes in the gas and simulated aqueous phase

Species	Functional	Phase	ΔE_{int}	ΔE_{Pauli}	ΔE_{elstat}	ΔE_{orb}	ΔE_{disp}	ΔE_{solv}	ΔE_{prep}	$-D_e$
cis$_1$-[OsO$_4$(OH)$_2$]$^{2-}$	PBE	Gas	32.8	176.9	−65.7	−78.5	—	—	18.3	51.1
		Aqueous	41.4	187.3	−70.8	−75.1	—	−64.4	11.6	−11.4
	PBE-D	Gas	32.1	173.0	−62.8	−77.5	−0.7	—	17.3	49.4
		Aqueous	40.0	183.0	−67.5	−74.1	−1.4	−64.6	11.4	−13.1
	PBE-D3	Gas	31.8	176.3	−65.2	−78.3	−1.0	—	18.1	50.0
		Aqueous	40.3	186.4	−70.2	−74.9	−1.0	−64.4	11.7	−12.4
	PBE-D3(BJ)	Gas	32.2	176.9	−65.5	−78.2	−1.1	—	18.0	50.2
		Aqueous	40.9	186.5	−70.1	−74.4	−1.1	−64.4	11.2	−12.3
	PBE-dDsC	Gas	32.0	178.6	−66.7	−78.5	−1.4	—	17.7	49.7
		Aqueous	40.9	187.0	−70.4	−74.5	−1.2	−64.4	11.0	−12.5
cis$_2$-[OsO$_4$(OH)$_2$]$^{2-}$	PBE	Gas	32.5	174.7	−64.6	−77.6	—	—	18.1	50.6
		Aqueous	40.1	185.0	−69.5	−75.4	—	−63.0	11.4	−11.5
	PBE-D	Gas	30.9	170.4	−61.7	−76.4	−1.4	—	17.9	48.7
		Aqueous	38.7	179.7	−65.5	−74.0	−1.5	−63.2	11.3	−13.2
	PBE-D3	Gas	31.4	173.8	−64.1	−77.3	−1.0	—	18.1	49.4
		Aqueous	38.8	183.0	−68.2	−75.0	−1.0	−63.0	11.7	−12.5
	PBE-D3(BJ)	Gas	31.6	174.9	−64.8	−77.5	−1.1	—	18.0	49.6
		Aqueous	39.3	184.4	−69.0	−75.1	−1.1	−62.9	11.3	−12.4
	PBE-dDsC	Gas	31.5	176.8	−66.0	−77.9	−1.4	—	17.7	49.2
		Aqueous	39.3	184.9	−69.3	−75.1	−1.2	−63.0	11.1	−12.6
trans-[OsO$_4$(OH)$_2$]$^{2-}$	PBE	Gas	17.5	227.4	−102.1	−107.8	—	—	42.7	60.2
		Aqueous	24.3	237.3	−109.0	−104.1	—	−65.1	37.8	−3.0
	PBE-D	Gas	16.4	226.5	−101.6	−107.6	−0.9	—	42.8	59.2
		Aqueous	23.0	234.7	−107.3	−103.4	−1.0	−65.4	38.5	−3.9
	PBE-D3	Gas	16.7	227.3	−102.1	−107.8	−0.7	—	42.7	59.4
		Aqueous	23.5	236.9	−108.8	−104.0	−0.8	−65.2	38.1	−3.6
	PBE-D3(BJ)	Gas	16.6	229.1	−103.3	−108.2	−1.0	—	42.6	59.3
		Aqueous	23.3	240.4	−111.2	−104.9	−1.0	−65.3	38.1	−3.8
	PBE-dDsC	Gas	16.6	230.8	−104.5	−108.6	−1.2	—	42.4	59.0
		Aqueous	23.5	241.0	−111.5	−105.0	−1.0	−65.3	37.8	−4.0

atoms to be chemically bonded, according to this theory, is based on the existence of a (3, −1) bond critical point (BCP) or a saddle point along a line of maximum electron density, ρ, also called an atomic interaction line (AIL) linking the nuclei of neighbouring atoms. At the BCP the gradient of the electron density vanishes, $\nabla\rho(\mathbf{r}) = 0$, and the sum of the three eigenvalues (λ_1 and λ_2 are negative, λ_3 is positive), obtained from the electron density Hessian matrix, known as the Laplacian, $\nabla^2\rho(\mathbf{r})_b$, may have either a net positive or negative value. A positive Laplacian value at the BCP indicates a local depletion of charge. This is indicative of an ionic (closed-shell) type of bonding. A negative Laplacian value is a sign of a local concentration of charge and is indicative of a shared/covalent interaction. However, a positive Laplacian value could in some cases be misleading, as the classification of the bond between two "closed-shell" interacting atoms is also determined by a second index, the total electronic energy density, E_b^e, at the BCP. This term is defined as the sum of the kinetic energy density, G_b, which usually dominates in a non-covalent bond, and the potential energy density, V_b, which is usually negative and is associated with accumulation of charge between the nuclei. In clearly covalent bonds both the $\nabla^2\rho(\mathbf{r})_b$ and $E_b^e = G_b + V_b$ are negative whilst the electron density at the BCP is larger than 0.1. In less clear cases, where the $\nabla^2\rho(\mathbf{r})_b$ has a relatively small positive value, the magnitude of E_b^e can be used to further classify the bond, from being slightly covalent to purely ionic, *e.g.* if $\nabla^2\rho > 0$ and E_b^e is negative the bond is called dative on the other hand if E_b^e is positive the bond is ionic. Moreover, the G_b/ρ_b ratio index is generally accepted to be less than unity for shared interactions and greater than unity for closed-shell interactions. The calculated BCP's electron density topology indices of all Os^{VIII} species in the simulated aqueous phase (PBE functional) are listed in Table S2† (see Table S3† for values obtained using PBE-D3(BJ) functional) and the molecular graphs obtained illustrated in Fig. 2.

The Laplacian at all the Os^{VIII}=O BCPs of all complexes, Table S2,† are positive, ranging from 0.76 to 0.86, and the G_b/ρ_b ratio is always more than unity, from 1.41 to 1.48, indicating ionic bonding interactions. Since the E_b^e is negative in all cases, from −0.16 to −0.11, the interaction has a slight covalent character. The ionicity of the bonding interactions is less in the case of the Os^{VIII}–OH BCPs in all the complexes. The Laplacian has a smaller positive value, from 0.30 to 0.38, while the G_b/ρ_b ratio is only slightly greater than unity, from 1.02 to 1.06. These results, along with the negative E_b^e values, from −0.05 to −0.03, qualify these interactions as polar covalent (dative) and corroborate the results obtained by the EDA analysis. The O–H bonding interactions are clearly covalent as indicated by the large negative Laplacian values, from −2.36 to −2.25, Fig. 4, and the large negative E_b^e values, from −0.67 to −0.66. The G_b/ρ_b ratio is also much smaller than unity, from 0.23 to 0.26. No qualitative changes are observed when topological analysis of the electron density is performed in the gas phase, Tables S4 and S5.† The Laplacian of the electron density, plotted along the Os^{VIII}–O–H plane of all four Os^{VIII} species, shown in Fig. 4, allows for the visualisation of

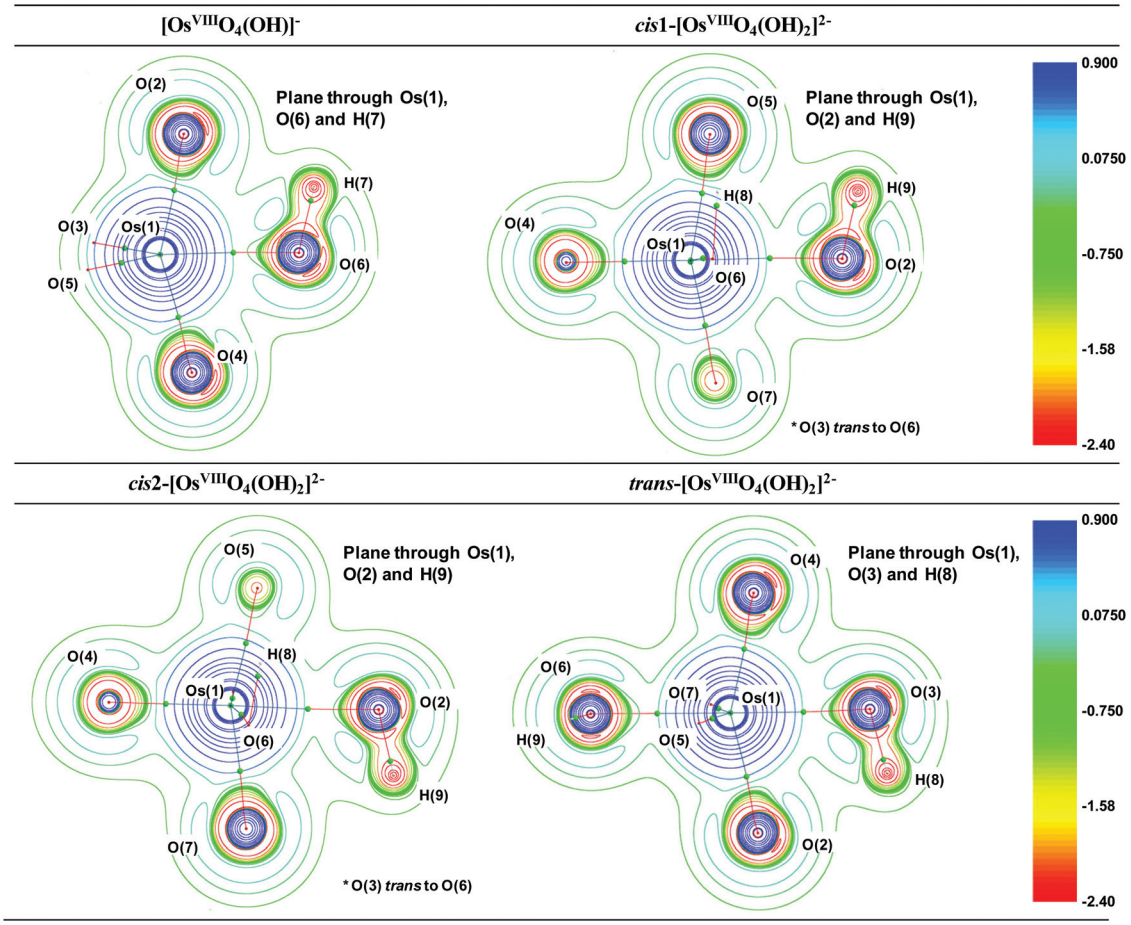

Fig. 4 The Laplacian of the electron density ($\nabla^2\rho$) of each of the Os^{VIII} oxo/hydroxido complexes in the simulated aqueous phase (PBE functional) with numbering scheme used in Table S2.† BCPs are indicated as small green spheres. Red and blue colouring corresponds to regions of local charge accumulation and depletion respectively.

the charge density distribution at an Os^{VIII}=O, Os^{VIII}–OH and O–H BCP which displays the relative ionic (blue), polar covalent (green) and covalent (red) character of their bonding interactions respectively. Moreover, it is evident from the molecular graphs obtained using QTAIM, Fig. 2, that no intramolecular bonding interactions between neighbouring hydroxido and oxo ligands in any of the Os^{VIII} species are present.

The more recent Non-Covalent Interactions (NCI) analysis method is frequently used to recognise and categorise intra- and intermolecular bonding interactions in a wide variety of chemical systems.[57] This is based on a 2D plot of the reduced density gradient (RDG), s, as a function of the sign of λ_2 multiplied with the electron density, ρ, eqn (16). A bonding interaction according to Johnson *et al.*,[57] *e.g.* hydrogen bonding or π–π stacking is characterised by an accumulation of electron density in a particular region in 3D space and in these cases $\lambda_2 < 0$. By contrast, repulsive interactions have a $\lambda_2 > 0$.

In a recent study, Cukrowski *et al.*[73] revealed that local properties of bonding, *i.e.* attractive or repulsive, based on the NCI interpretation of the electron density topology do not necessarily correlate with the physical nature of that interaction. The authors further concluded that NCI reveals only the presence or absence of possible interactions between atoms and electron density accumulation or depletion. However, in many chemical systems of less ambiguity, NCI analyses can be successfully used to identify attractive or repulsive interactions as will be shown in the following text.

$$s = \frac{1}{2(3\pi^2)^{1/3}} \frac{|\nabla\rho|}{\rho^{4/3}} \quad (16)$$

Points where $s = 0$ correspond to BCPs due to annihilation of the density gradient. A non-covalent interactions (NCI) analysis of the five-coordinate $[Os^{VIII}O_4(OH)]^-$ species, Fig. 5, indicates that a relatively weak stabilisation is present between neighbouring oxo and hydroxido ligands. Although the trough at approximately $\text{sign}(\lambda_2)\rho \approx -0.03$ au does not terminate at RDG of zero, a weak attractive intramolecular hydrogen bonding interaction between H(7) & O(2) is present. The trough corresponding to this interaction is visualised in 3D space in Fig. 5(b) as a red region. The four troughs between

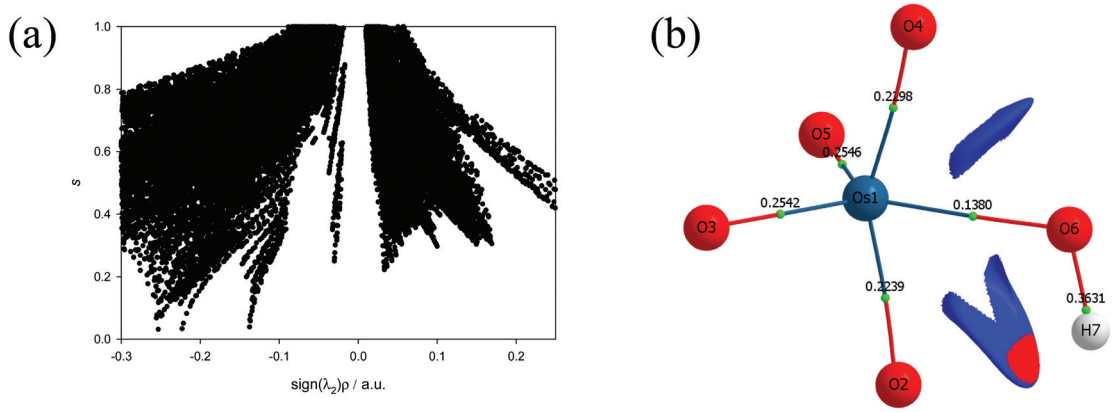

Fig. 5 (a): Plot of the reduced density gradient s and sign(λ_2)ρ of $[Os^{VIII}O_4(OH)]^-$ in the simulated aqueous phase (PBE functional). (b): Taking the positions of the troughs at approximately −0.025 into account, the plotted NCI isosurface corresponding to cut-off values of s = 0.6 au and 0.03 < ρ < 0.01 au captures the intramolecular stabilisation interaction. Red and blue colouring corresponds to regions of negative and positive λ_2 values respectively. Electron density values, ρ_b, at the BCPs are included.

−0.25 and −0.22 au are due to ionic (closed-shell) Os^{VIII}=O bonds while the trough at −0.14 au is due to the polar covalent (dative) Os^{VIII}–OH bond and these correspond with the BCPs found in the abovementioned QTAIM analysis. It is also evident that there are troughs with positive λ_2 values that do not extend to a RDG of zero. These troughs are also visualised in 3D space Fig. 5(b) as blue regions and are indicative of repulsive interactions between oxygen moieties, O(4) & O(6) and O(6) & O(2), of neighbouring ligands.

The NCI analyses of the *cis*$_1$-$[Os^{VIII}O_4(OH)_2]^{2-}$, *cis*$_2$-$[Os^{VIII}O_4(OH)_2]^{2-}$ and *trans*-$[Os^{VIII}O_4(OH)_2]^{2-}$ species indicate relatively weak intramolecular hydrogen bonding interactions between neighbouring oxo and hydroxido ligands, Fig. 6. Both the hydroxido hydrogens in each of the three complexes have weak intramolecular hydrogen bonding interactions with a neighbouring oxo ligand. The troughs at sign(λ_2)ρ range from −0.02 to −0.04 au are due to these attractive interactions and are visualised in 3D space in Fig. 6 as red regions. Several more repulsive interactions between oxygen moieties of neighbouring ligands are also present compared to the coordinatively unsaturated five-coordinate $[Os^{VIII}O_4(OH)]^-$ complex anion.

Overall, the PBE and dispersion-corrected PBE functionals yielded good agreement with experimentally determined ΔG°_{rxn} values, Tables 4 and 7. A graphical assessment of how well these DFT-calculated equilibrium constants of reactions (3) and (4) compare to the experimentally obtained values is shown in Fig. 7 where the Os^{VIII} species distribution as a function of hydroxide concentration is plotted. For clarity, only the data for the PBE and PBE-D3 functionals are shown as examples.

Kinetics of coordination sphere expansion reactions (3) & (4)

It is found experimentally that when a neutral aqueous Os^{VIII} solution is mixed with a relatively concentrated hydroxide solution that a rapid colour change occurs due to coordination sphere expansion reactions (3) & (4). Stopped-flow kinetics experiments were performed at 298.15 K in an attempt to quantify the rate at which these reactions occur. However, the spectral change occurs in such a small time scale that a 'constant' absorbance *versus* time signal is obtained, *i.e.* the expected absorbance when Os^{VIII} is present at equilibrium in 2.0 M hydroxide is already observed at the first data point, at 0.001 seconds, which corresponds to the earliest possible reading that the instrument is capable of making. This indicates that the activation Gibbs energy barriers for the coordination sphere expansion reactions are relatively low. A computational study was subsequently performed to ascertain the mechanism of coordination sphere expansion and to obtain reaction energy barriers, *i.e.* does hydroxide coordinate directly to $Os^{VIII}O_4$ and then to $[Os^{VIII}O_4(OH)]^-$ in two, consecutive, elementary reaction steps as depicted in eqn (3) and (4)? From Fig. 8(a) it can be seen that the $Os^{VIII}O_4$ species' electrostatic surface potential defined at the 0.03 au electron density the Os^{VIII} atom has four σ-holes[75] of equal magnitude, *i.e.* regions where the Os atom has less electron density compared to neighbouring regions. For this reason a linear transit, relaxed scan, calculation in which a hydroxide ligand was incrementally moved closer to one of the four Os^{VIII} σ-holes was performed. The relaxed scan calculations were only done in the simulated aqueous phase. The structure found at the maximum of the potential energy surface was subsequently submitted for a transition state search. The converged geometry structure where the Os^{VIII}–OH distance is 3.43 Å, Fig. 8(b), has one negative vibrational frequency, corresponding to a saddle point on the PES and one degree of freedom, where the hydroxide oxygen atom vibrates towards and back w.r.t. the Os^{VIII} atom. The Gibbs energies of activation of the forward and reverse reactions, eqn (3), and their associated rate constants were calculated using eqn (17), and are listed in Table 9.

$$k(T) = \kappa \frac{k_B T}{hc^\circ} e^{-\Delta^\ddagger G^\circ/RT} \quad (17)$$

It is assumed that the transmission factor or transmission coefficient, κ, is equal to one and do not vary as a function of

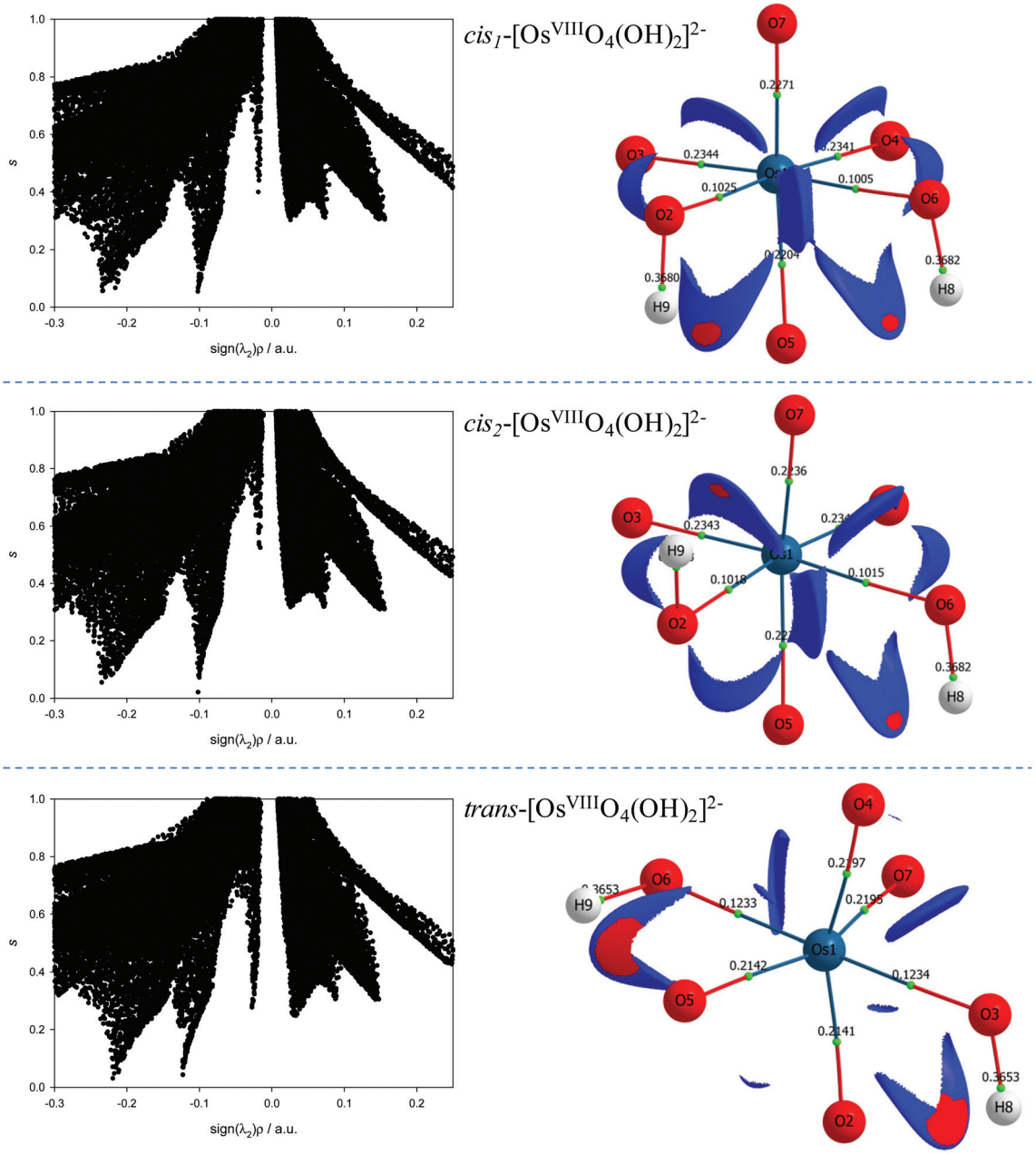

Fig. 6 Left: Plots of the reduced density gradient s and sign(λ_2)ρ of the cis_1-(top), cis_2-(middle) and *trans*-(bottom) $[Os^{VIII}O_4(OH)_2]^{2-}$ complexes in the simulated aqueous phase (PBE functional). Right: Taking the positions of the troughs at approximately −0.025 into account, plotted NCI isosurfaces corresponding to cut-off values of s = 0.6 au and 0.03 < ρ < 0.01 au captures the respective intramolecular stabilisation interactions. Red and blue colouring corresponds to regions of negative and positive λ_2 values respectively. Electron density values, ρ_b, at the BCPs are included.

temperature. The rate constants obtained of reaction (3) are relatively large and falls in the range of a diffusion-controlled rate-limiting step.[76]

From Fig. 8(c) it is observed that the $[Os^{VIII}O_4(OH)]^-$ species has two equivalent σ-holes. In a similar fashion to the method used to describe the mechanism of reaction (3), the "incoming" hydroxido ligand was placed in line with the Os^{VIII} atom σ-hole and a linear transit relaxed scan calculation was performed. The transition state geometry structure where the Os^{VIII}–OH distance is 3.22 Å, Fig. 8(d), has one negative vibrational frequency. Reactions (3) & (4) occur as two elementary steps. The Gibbs energies of activation of the forward and reverse reactions, eqn (4) (or more specifically reaction (13)), and their associated rate constants were calculated using eqn (17) and are listed in Table 10.

The calculated rate constants obtained for reaction (13), Table 10, are relatively large, yet on estimation an order of magnitude less when compared to reaction (3). We attribute

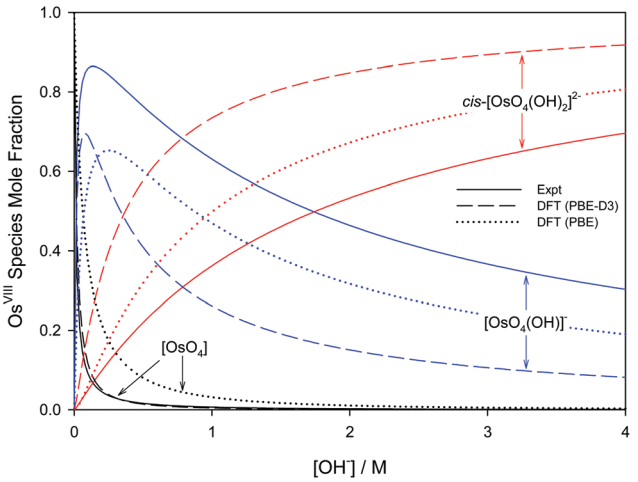

Fig. 7 Species distribution diagram of $[OsO_4(OH)_n]^{n-}$ (n = 0, 1, 2) as a function of hydroxide concentration as calculated from DFT (PBE and PBE-D3 functionals) in contrast to experiment.[74]

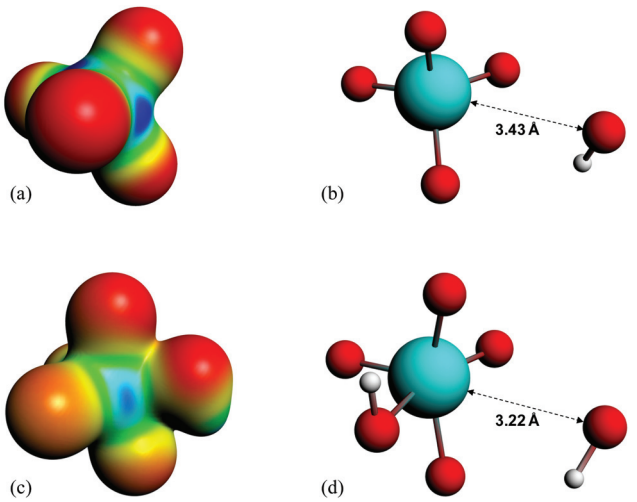

Fig. 8 (a) and (c): Electrostatic surface potential maps of the optimised geometries of $Os^{VIII}O_4$ and $[Os^{VIII}O_4(OH)]^-$ in the simulated aqueous phase (PBE functional) corresponding to a density isosurface value of 0.03 au. Negatively and positively charged regions are indicated by red and blue colouring, respectively. (b) and (d): Molecular graphs of the calculated transition state structures (PBE functional) of reactions (3) & (4), respectively.

Table 9 Calculated Gibbs Free Energies of activation in kcal mol^{-1} and rate constants of reaction (3) at 298.15 K where k_1 and k_{-1} are the forward and reverse rate constants respectively

Functional	$\Delta^{\ddagger}G^{\circ}_{forward}$	k_1 (L mol^{-1} s^{-1})	$\Delta^{\ddagger}G^{\circ}_{reverse}$	k_{-1} (s^{-1})
PBE	6.6	9.2×10^7	8.2	6.2×10^6
PBE-D	6.1	2.1×10^8	7.3	2.8×10^7
PBE-D3	5.9	2.9×10^8	8.3	4.8×10^6
PBE-D3(BJ)	7.1	4.2×10^7	10.1	2.6×10^5
PBE-dDsC	7.3	2.7×10^7	10.2	2.2×10^5

Table 10 Calculated Gibbs Free Energies of activation in kcal mol^{-1} and rate constants of reaction (13) at 298.15 K where k_2 and k_{-2} are the forward and reverse rate constants respectively

Functional	$\Delta^{\ddagger}G^{\circ}_{forward}$	k_2 (L mol^{-1} s^{-1})	$\Delta^{\ddagger}G^{\circ}_{reverse}$	k_{-2} (s^{-1})
PBE	11.7	1.5×10^4	11.8	1.5×10^4
PBE-D	7.8	1.2×10^7	10.4	1.5×10^5
PBE-D3	10.8	7.4×10^4	11.4	2.6×10^4
PBE-D3(BJ)	10.5	1.3×10^5	11.4	2.5×10^4
PBE-dDsC	10.5	1.4×10^5	11.6	2.0×10^4

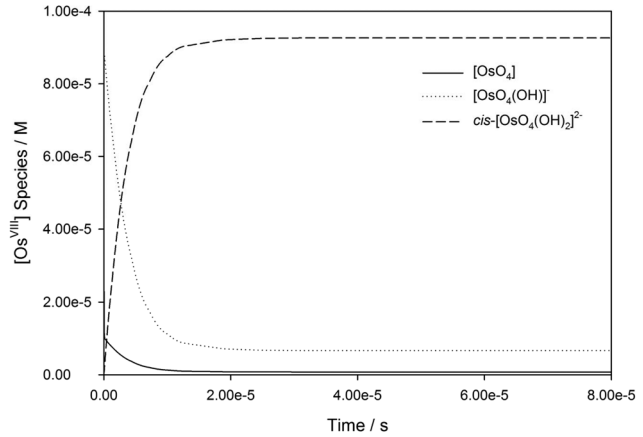

Fig. 9 Simulated kinetic traces of $Os^{VIII}O_4$ reacting with OH^- in 2 M NaOH as a function of time (PBE-dDsC functional).

this result in part to the repulsion between the two negatively charged species which increases the $\Delta^{\ddagger}G^{\circ}$ activation energy barrier. From reactions (3) and (13), the rate law eqn (18)–(20) are derived. Using the rate constants obtained with the PBE-dDsC functional, the species concentration evolution curves as a function of time were calculated, Fig. 9. The initial conditions in this hypothetical "stopped-flow" kinetics calculation are two aqueous solutions of equal volume where one syringe contains $Os^{VIII}O_4$ at 10.0 mM and the other contains 4.0 M $[OH]^-$. It is seen in Fig. 9 that reactions (3) and (13) reach equilibrium in less than 0.00003 seconds which explains our experimental stopped-flow kinetics results.

$$\frac{d[OsO_4]}{dt} = -k_1[OsO_4][OH^-] + k_{-1}[OsO_4(OH)^-] \quad (18)$$

$$\frac{d[OsO_4(OH)^-]}{dt} = k_1[OsO_4][OH^-] - k_{-1}[OsO_4(OH)^-] - k_2[OsO_4(OH)^-][OH^-] + k_{-2}cis\text{-}[OsO_4(OH)_2{}^{2-}] \quad (19)$$

$$\frac{d cis\text{-}[OsO_4(OH)_2{}^{2-}]}{dt} = k_2[OsO_4(OH)^-][OH^-] - k_{-2}cis\text{-}[OsO_4(OH)_2{}^{2-}] \quad (20)$$

Conclusions

We have demonstrated that DFT computational methodologies, mainly with GGA functionals, are successful in elucidating the equilibrium structures and energies of Os^{VIII} oxo/hydroxido species that are present in aqueous basic solutions. Our calculations provide evidence that the Os^{VIII} species present in basic aqueous solutions are $Os^{VIII}O_4$, $[Os^{VIII}O_4(OH)]^-$ and two *cis*-$[Os^{VIII}O_4(OH)_2]^{2-}$ complexes and that water-bonded Os^{VIII} species most likely do not exist. Good agreement with reported, experimentally obtained ΔG°_{rxn} values pertaining to the two coordination sphere expansion reactions validates the DFT methodology used. The thermodynamic driving force of the first coordination sphere expansion reaction is the bonding energy of the Os^{VIII}–OH metal-hydroxido ligand present in $[Os^{VIII}O_4(OH)]^-$ and of the second reaction it is the larger hydration energy of the doubly-charged *cis*-$[Os^{VIII}O_4(OH)_2]^{2-}$ species in comparison with that of the two, singly-charged reactants. Both coordination sphere expansion reactions have relatively low transition state energy, $\Delta^\ddagger G^\circ$, barriers.

QTAIM and EDA analyses indicate that Os^{VIII}=O bonding interactions are ionic (closed-shell) whereas the Os^{VIII}–OH bonding interactions are polar covalent (dative). NCI analysis of both the $[Os^{VIII}O_4(OH)]^-$ and *cis*-$[Os^{VIII}O_4(OH)_2]^{2-}$ species indicate the presence of weak intramolecular hydrogen bonding interactions between neighbouring oxo and hydroxido ligands.

The results obtained in this study allow for subsequent investigations which aim to describe the mechanism of the proposed comproportionation reaction by Gerber *et al.*[11] Furthermore, the clarity w.r.t. the Os^{VIII} speciation can now be used to make informed suggestions regarding which Os^{VIII} complexes are the active catalysts in future studies done in aqueous solutions.

References

1 A. Dehestani, W. H. Lam, D. A. Hrovat, E. R. Davidson, W. T. Borden and J. M. Mayer, *J. Am. Chem. Soc.*, 2005, **127**, 3423.
2 Z. M. Galbács, A. Zsednai and L. J. Csányi, *Transition Met. Chem.*, 1983, **8**, 328.
3 B. J. McFadzean, PhD Dissertation, NMMU, South Africa, 2008.
4 A. H. Éll, A. Closson, H. Adolfsson and J.-E. Bäckvall, *Adv. Synth. Catal.*, 2003, **345**, 1012.
5 S. M. Desai, N. N. Halligudi and S. T. Nandibewoor, *Int. J. Chem. Kinet.*, 1999, **31**, 583.
6 N. P. Shetti, R. R. Hosamani and S. T. Nandibewoor, *Res. Lett. Inorg. Chem.*, 2008, **216058**, 1.
7 K. Byadagi, M. Meti, S. Nandibewoor and S. Chimatadar, *Ind. Eng. Chem. Res.*, 2013, **52**, 9011.
8 M. P. Singh, H. S. Singh, M. C. Gangwar, P. Thakur and A. K. Singh, *Proc. - Indian Acad. Sci., Sect. A*, 1975, **41**, 178.
9 N. N. Ivan-Emin, N. A. Nevskaya, N. N. Nevskii and A. S. Izmailovich, *Russ. J. Inorg. Chem.*, 1984, **29**, 710.
10 H. C. Jewiss, W. Levason, M. Tajik, M. Webster and N. P. C. Walker, *J. Chem. Soc., Dalton Trans.*, 1985, 199.
11 T. E. Geswindt, W. J. Gerber, H. E. Rohwer and K. R. Koch, *Dalton Trans.*, 2011, **40**, 8581.
12 W. P. Griffith, *The Chemistry of the Rarer Platinum Metals (Os, Ru, Ir & Rh)*, Interscience, 1967, ch. 3.
13 B. Krebs and K. D. Hasse, *Acta Crystallogr., Sect. B: Struct. Crystallogr. Cryst. Chem.*, 1976, **32**, 1334.
14 N. N. Nevskii, B. Ivan-Emin, O. N. A. Nevskaya and N. V. Belov, *Dokl. Akad. Nauk SSSR*, 1983, **226**, 245.
15 Z. Y. Lin and M. B. Hall, *Coord. Chem. Rev.*, 1993, **123**, 149.
16 D. T. Richens, *The Chemistry of Aqua Ions*, John Wiley and Sons, New York, 1997.
17 D. W. Nelson, A. Gypser, P. T. Ho, H. C. Kolb, T. Kondo, H.-L. Kwong, A. McGrath, E. A. Rubin, P.-O. Norbby, K. P. Gable and K. B. Sharpless, *J. Am. Chem. Soc.*, 1997, **119**, 1840.
18 C. J. Cramer and D. G. Truhlar, *Phys. Chem. Chem. Phys.*, 2009, **11**, 10757.
19 G. te Velde, F. M. Bickelhaupt, S. J. A. van Gisbergen, C. Fonseca Guerra, E. J. Baerends, J. G. Snijders and T. Ziegler, *J. Comput. Chem.*, 2001, **22**, 931.
20 C. Fonseca Guerra, J. G. Snijders, G. te Velde and E. J. Baerends, *Theor. Chem. Acc.*, 1998, **99**, 391.
21 E. J. Baerends, J. Autschbach, D. Bashford, A. Bérces, F. M. Bickelhaupt, C. Bo, P. M. Boerrigter, L. Cavallo, D. P. Chong, L. Deng, R. M. Dickson, D. E. Ellis, M. van Faassen, L. Fan, T. H. Fischer, C. Fonseca Guerra, A. Ghysels, A. Giammona, S. J. A. van Gisbergen, A. W. Götz, J. A. Groeneveld, O. V. Gritsenko, M. Grüning, F. E. Harris, P. van den Hoek, C. R. Jacob, H. Jacobsen, L. Jensen, G. van Kessel, F. Kootstra, M. V. Krykunov, E. van Lenthe, D. A. McCormack, A. Michalak, M. Mitoraj, J. Neugebauer, V. P. Nicu, L. Noodleman, V. P. Osinga, S. Patchkovskii, P. H. T. Philipsen, D. Post, C. C. Pye, W. Ravenek, J. I. Rodríguez, P. Ros, P. R. T. Schipper, G. Schreckenbach, M. Seth, J. G. Snijders, M. Solà, M. Swart, D. Swerhone, G. te Velde, P. Vernooijs, L. Versluis, L. Visscher, O. Visser, F. Wang, T. A. Wesolowski, E. M. van Wezenbeek, G. Wiesenekker, S. K. Wolff, T. K. Woo, A. L. Yakovlev and T. Ziegler, *ADF2012.02*, SCM, Theoretical Chemistry, Vrije Universiteit, Amsterdam, The Netherlands, http:/www.scm.com.
22 E. van Lenthe, E. J. Baerends and J. G. Snijders, *J. Chem. Phys.*, 1993, **99**, 4597.
23 E. van Lenthe, E. J. Baerends and J. G. Snijders, *J. Chem. Phys.*, 1994, **101**, 9783.
24 E. van Lenthe, A. E. Ehlers and E. J. Baerends, *J. Chem. Phys.*, 1999, **110**, 8943.
25 E. van Lenthe, J. G. Snijders and E. J. Baerends, *J. Chem. Phys.*, 1996, **105**, 6505.
26 E. van Lenthe, R. van Leeuwen, E. J. Baerends and J. G. Snijders, *Int. J. Quantum Chem.*, 1996, **57**, 281.
27 S. H. Vosko, L. Wilk and M. Nusair, *Can. J. Phys.*, 1980, **58**(8), 1200.

28 J. P. Perdew, K. Burke and M. Ernzerhof, *Phys. Rev. Lett.*, 1996, **77**, 3865.
29 C. Adamo and V. Barone, *J. Chem. Phys.*, 1996, **116**, 5933.
30 S. Grimme, *J. Comput. Chem.*, 2006, **27**, 1787.
31 S. Grimme, J. Anthony, S. Ehrlich and H. Krieg, *J. Chem. Phys.*, 2010, **132**, 154104.
32 S. Grimme, S. Ehrlich and L. Goerigk, *J. Comput. Chem.*, 2011, **32**, 1457.
33 S. N. Steinmann and C. Corminboeuf, *J. Chem. Theor. Comput.*, 2011, **7**, 3567.
34 A. D. Becke, *Phys. Rev. A*, 1988, **38**, 3098.
35 C. Lee, W. Yang and R. G. Parr, *Phys. Rev. B: Condens. Matter*, 1988, **37**, 785.
36 B. G. Johnson, P. M. W. Gill and J. A. Pople, *J. Chem. Phys.*, 1993, **98**, 5612.
37 T. V. Russo, R. L. Martin and P. J. Hay, *J. Chem. Phys.*, 1994, **101**, 7729.
38 J. P. Perdew, J. A. Chevary, S. H. Vosko, K. A. Jackson, M. R. Pederson, D. J. Sing and C. Fiolhais, *Phys. Rev. B: Condens. Matter*, 1992, **46**, 6671.
39 Y. Zhao and D. G. Truhlar, *J. Chem. Phys.*, 2006, **125**, 194101.
40 Y. Zhao and D. G. Truhlar, *Theor. Chem. Acc.*, 2008, **120**, 215.
41 E. van Lenthe and E. J. Baerends, *J. Comput. Chem.*, 2003, **24**, 1142.
42 C. C. Pye and T. Ziegler, *Theor. Chem. Acc.*, 1999, **101**, 396.
43 A. Klamt and G. Schüürmann, *J. Chem. Soc., Perkin Trans. 2*, 1993, 799.
44 A. Klamt, *J. Phys. Chem.*, 1995, **99**, 2224.
45 A. Klamt and V. Jones, *J. Chem. Phys.*, 1996, **105**, 9972.
46 A. Bérces, R. M. Dickson, L. Fan, H. Jacobsen, D. Swerhone and T. Ziegler, *Comput. Phys. Commun.*, 1997, **100**, 247.
47 H. Jacobsen, A. Bérces, D. Swerhone and T. Ziegler, *Comput. Phys. Commun.*, 1997, **100**, 263.
48 S. K. Wolff, *Int. J. Quantum Chem.*, 2005, **104**, 645.
49 L. Fan and T. Ziegler, *J. Chem. Phys.*, 1992, **96**, 9005.
50 L. Fan and T. Ziegler, *J. Phys. Chem.*, 1992, **96**, 6937.
51 T. Ziegler and A. Rauk, *Inorg. Chem.*, 1979, **18**, 1558.
52 T. Ziegler and A. Rauk, *Inorg. Chem.*, 1979, **18**, 1755.
53 M. Mitoraj, A. Michalak and T. Ziegler, *J. Chem. Theor. Comput.*, 2009, **5**, 962.
54 *GUI 2014*, SCM, Amsterdam, The Netherlands, http://www.scm.com.
55 J. I. Rodríguez, R. F. W. Bader, P. W. Ayers, C. Michel, A. W. Götz and C. Bo, *Chem. Phys. Lett.*, 2009, **472**, 149.
56 J. I. Rodríguez, *J. Comput. Chem.*, 2013, **34**, 681.
57 E. R. Johnson, S. Keinan, P. Mori-Sanchez, J. Contreras-Garcia, A. J. Cohen and W. Yang, *J. Am. Chem. Soc.*, 2010, **132**, 6498.
58 T. A. Keith, *AIMAll (Version 15.05.18)*, TK Gristmill Software, Overland Park KS, USA, 2015 (aim.tkgristmill.com).
59 M. J. Frisch, G. W. Trucks, H. B. Schlegel, G. E. Scuseria, M. A. Robb, J. R. Cheeseman, G. Scalmani, V. Barone, B. Mennucci, G. A. Petersson, H. Nakatsuji, M. Caricato, X. Li, H. P. Hratchian, A. F. Izmaylov, J. Bloino, G. Zheng, J. L. Sonnenberg, M. Hada, M. Ehara, K. Toyota, R. Fukuda, J. Hasegawa, M. Ishida, T. Nakajima, Y. Honda, O. Kitao, H. Nakai, T. Vreven, J. A. Montgomery Jr., J. E. Peralta, F. Ogliaro, M. Bearpark, J. J. Heyd, E. Brothers, K. N. Kudin, V. N. Staroverov, T. Keith, R. Kobayashi, J. Normand, K. Raghavachari, A. Rendell, J. C. Burant, S. S. Iyengar, J. Tomasi, M. Cossi, N. Rega, J. M. Millam, M. Klene, J. E. Knox, J. B. Cross, V. Bakken, C. Adamo, J. Jaramillo, R. Gomperts, R. E. Stratmann, O. Yazyev, A. J. Austin, R. Cammi, C. Pomelli, J. W. Ochterski, R. L. Martin, K. Morokuma, V. G. Zakrzewski, G. A. Voth, P. Salvador, J. J. Dannenberg, S. Dapprich, A. D. Daniels, O. Farkas, J. B. Foresman, J. V. Ortiz, J. Cioslowski and D. J. Fox, *Gaussian 09 (Revision D.01)*, Gaussian, Inc., Wallingford CT, 2013.
60 P. J. Hay and W. R. Wadt, *J. Chem. Phys.*, 1985, **82**, 270.
61 W. R. Wadt and P. J. Hay, *J. Chem. Phys.*, 1985, **82**, 284.
62 P. J. Hay and W. R. Wadt, *J. Chem. Phys.*, 1985, **82**, 299.
63 T. H. Dunning Jr., *J. Chem. Phys.*, 1989, **90**, 1007.
64 V. Barone and M. Cossi, *J. Phys. Chem. A*, 1998, **102**, 1995.
65 M. Cossi, N. Rega, G. Scalmani and V. Barone, *J. Comput. Chem.*, 2003, **24**, 669.
66 E. J. Wells, A. D. Jordan, D. S. Alderdice and I. G. Ross, *Aust. J. Chem.*, 1967, **20**, 2315.
67 J. L. Roebber, R. N. Wiener and C. A. Russel, *J. Chem. Phys.*, 1974, **60**, 3166.
68 R. S. McDowell and M. Goldblatt, *Inorg. Chem.*, 1971, **10**(3), 625.
69 H. M. Seip and R. Stølevik, *Acta Chem. Scand.*, 1966, **20**, 385.
70 R. F. W. Bader, *Atoms in Molecules. A Quantum Theory*, Oxford University Press, Oxford, 1990.
71 M. von Hopffgarten and G. Frenking, *WIREs Comput. Mol. Sci.*, 2012, **2**, 43.
72 Y. Jeanvoine, P. Miró, F. Martelli, C. J. Cramer and R. Spezia, *Phys. Chem. Chem. Phys.*, 2012, **14**, 14822.
73 I. Cukrowski, J. H. de Lange, A. S. Adeyinka and P. Mangondo, *Comput. Theor. Chem.*, 2015, **1053**, 60.
74 E. C. Hosten, *Complex Species Distribution (version 3.1)*, NMMU.
75 T. Clark, M. Hennemann, J. S. Murray and P. Politzer, *J. Mol. Model.*, 2007, **13**, 291.
76 O. von Berg and P. H. von Hippel, *Ann. Rev. Biophys. Chem.*, 1985, **14**, 131.